Predicting Thermochemical Equilibria with Interacting Defects: Sr$_{1-x}$Ce$_x$MnO$_{3-\delta}$ Alloys for Water Splitting

Anuj Goyal,[1,2] Michael D. Sanders,[3] Ryan P. O'Hayre,[3] and Stephan Lany[1,*]

[1] *National Renewable Energy Laboratory, Golden, Colorado 80401, USA*
[2] *Indian Institute of Technology Hyderabad, Kandi, Sangareddy, Telangana, 502284, India*
[3] *Colorado School of Mines, Golden, Colorado 80401, USA*

Solar thermochemical hydrogen is one of the few potential routes towards direct fuel production from renewable energy sources, but the thermodynamic boundary conditions for efficient and economic energy conversion are challenging. Success or failure of a given oxide working material depends on the subtle balance between enthalpy and entropy contributions in the redox processes. Developing a mechanistic understanding of the behavior of materials on the basis of atomistic models and first-principles calculations is an important part of advancing the technology. One challenge is to quantitatively predict thermochemical equilibria at high concentrations when the redox-active defects start to interact with each other, thereby impeding the formation of additional defects. This problem is of more general importance to applications that rely on high levels of off-stoichiometry or doping, including, for example, batteries, thermoelectrics, and ceramic fuel cells. To account for such repulsive defect interactions, we introduce a statistical mechanics approach, defining an expression for the free energy of defect interaction based on limited sampling of defect configurations in density functional theory supercell calculations. The parameterization of this energy contribution as a function of defect concentration and temperature allows on-the-fly simulation of thermochemical equilibria. The approach consistently incorporates finite temperature effects by including the leading contributions to the temperature-dependent free energy for the case at hand, i.e., the ideal gas and configurational enthalpies and entropies. We demonstrate the capability and utility of the approach by simulating the water splitting redox processes for Sr$_{1-x}$Ce$_x$MnO$_{3-\delta}$ alloys.

I. INTRODUCTION

Current renewable energy additions are dominated by electricity-producing sources such as photovoltaics and wind, but only 20% of the global final energy consumption occurs via electricity, with the lion's share being consumed in the form of fuels [1]. Thus, completing the energy transition with current technologies would require either total electrification or the availability of large excess capacities in renewable electricity that could be converted into fuels, e.g., by electrolysis [2]. Solar thermochemical hydrogen (STCH) is one of the few known potential routes towards direct renewable fuel production on an industrial scale [3], and it could provide an important alternative to electricity-based generation of fuels [4,5]. The two-step STCH redox cycle uses oxides that release oxygen under high-temperature reducing conditions (e.g., 1400 °C at O$_2$ partial pressure (pO$_2$) of 10^{-4} bar) and reoxidize in the presence of H$_2$O steam at lower but still elevated temperature (e.g., 850 °C at pH$_2$O = 1 bar) to split water and produce H$_2$ [6]. In many STCH systems, the reduction involves the formation of O vacancy (V_O) defects, and the viability of the process depends sensitively on the free energy of defect formation. The undesirable need for very high reduction temperatures in the prototypical STCH oxide CeO$_2$ has spurred efforts to design and discover new oxide materials. These efforts have borne some successes, leading to the discoveries of, for example, Sr- and Mn-doped LaAlO$_3$ [7], Ba$_4$CeMn$_3$O$_{12}$ [8], polycation oxides [9], CaTi$_{0.5}$Mn$_{0.5}$O$_3$ [10], and (Ca, Ce)(Ti, Mn)O$_3$ [11,12]. However, STCH is still held back by material limitations, especially regarding the severe decline in H$_2$ yield with increasing H$_2$:H$_2$O ratio during the oxidation step. Inspired by Ba$_4$CeMn$_3$O$_{12}$, where Ce partially replaces Mn in BaMnO$_3$ to form a line compound, recent interest

was directed at Ce-doped Sr_2MnO_4 and Ce-doped $SrMnO_3$ (SCM), which form tunable solid solutions, instead [13,14].

At this early stage of STCH technology, theory plays an important role, as it can help in two ways: (1) discovery of materials, i.e., searching for oxides with favorable STCH properties [15–18]; and (2) quantitative performance predictions, i.e., modeling reduction and oxidation behavior to predict the hydrogen production capability of promising candidates [19,20]. The thermodynamic window of opportunity for STCH is rather narrow, and subtle variations in the behavior of materials can be decisive. In addition to general material stability considerations, the STCH viability depends on the oxygen defect redox mechanism and the associated reduction enthalpies and entropies [21,22]. In turn, these thermodynamic parameters depend on formation energies and charge states of oxygen vacancy defects, as well as their interactions with each other and with other defects.

Thermochemical redox processes can be predicted from defect equilibria on the basis of first-principles supercell calculations of defect formation energies. In many cases, interactions of defects are mediated via exchange of electrons between each other and with the band continuum, which can be accounted for by a Fermi level dependence of the formation energies in conjunction with a charge neutrality condition [23–25]. Attractive forces between defects or dopants, e.g., between oppositely charged donor and acceptor defects, causes the formation of pairs and complexes that can be incorporated in defect equilibria with use of the corresponding binding energies and the law of mass action [26,27]. These concepts have been used to describe compositionally complex systems beyond the dilute limit, where cosubstitution increases the solubility limit of the individual dopants, often by orders of magnitude [20,27–29]. In addition, defect formation in disordered systems such as alloys introduces a distribution of formation energies, which can be either directly evaluated or expressed by an "effective formation energy" [25,30,31].

To support a sufficient hydrogen production capacity, STCH oxides must form high concentrations of a single type of defect—O vacancies—during thermochemical reduction. In contrast to the situation of attractive forces between different types of defect described above, we expect in this case that the formation of additional vacancies is increasingly impeded as their concentration rises. Therefore, quantitative modeling beyond the dilute limit must account for *repulsive* defect interactions. In principle, this task can be performed via lattice Monte Carlo methods, but the statistical sampling requirements limit or preclude the direct use of first-principles energies, e.g., from density functional theory (DFT). Instead, this approach generally requires the fitting of a model Hamiltonian, such as a cluster-expansion Hamiltonian [32], which, apart from the additional effort, also introduces an additional uncertainty in the total energy expression. Alternatively, here we incorporate the repulsive interaction energies in thermodynamic modeling of defect equilibria. A first step in this direction was taken in Refs. [31,33], where calculations with different supercell sizes were used to determine a concentration-dependent formation energy for a uniform oxygen vacancy distribution.

To account for the configurational degrees of freedom as well as the enthalpy and entropy contributions arising from nonuniform defect distributions, here we define a free energy of defect interaction ΔG_D^{int}. The corresponding partition sum is obtained from sampling of DFT supercell calculations. To approximate the full configuration space, we consider all nonequivalent O vacancy distributions that can be represented by pairs and triplets under periodic boundary conditions within a range of different cell sizes. This approach provides a unified picture for distributions of formation energies resulting from defect interactions and from disorder. Using a temperature-dependent parameterization of ΔG_D^{int} as a function of δ and x in $Sr_{1-x}Ce_xMnO_{3-\delta}$, we obtain defect equilibria for the thermochemical reduction of SCM in good agreement with experimental data. We then use the defect model to predict the water splitting redox cycle for SCM.

II. RESULTS AND DISCUSSION

A. Role of total energy functionals

The quantitative prediction of total energies in transition metal oxides remains challenging. Standard DFT usually requires augmentation with nonlocal potentials, as in the DFT with the Hubbard U parameter (DFT+U) [34] and hybrid functional [35] approaches, to obtain even qualitatively meaningful solutions [36,37]. Even then, however, a quantitative total energy prediction is still not guaranteed, as strikingly illustrated in the polymorphic energy ordering of MnO and CoO when compared with accurate many-body theory methods such as the random-phase approximation and the diffusion quantum Monte Carlo method [38,39]. In Sec. III, we present a careful analysis of different total energy functionals. Under specific consideration of the relative stability of the Mn^{4+}/Mn^{3+} and Ce^{4+}/Ce^{3+} oxidation states in binary bulk oxides, and through a comparative study of V_O defect formation energies in $SrMnO_3$, we find that the strongly constrained and appropriately normalized (SCAN) [40] + U [41] functional approach with $U_{Mn\,d} = 2$ eV and $U_{Ce\,f} = 1$ eV is best suited for obtaining accurate absolute O defect formation energies. The results presented in Sec. II were obtained with this functional. Notably, recent defect calculations in $FeAl_2O_4$ found very good agreement between DFT+U, hybrid functional, and random-phase approximation calculations [20]. However, such agreement should

TABLE I. Calculated atomic structures and vacancy formation energies in $SrMnO_3$ for the different O sites in the orthorhombic ground state of the hexagonal phase and in the metastable cubic perovskite phase. The table gives the relative multiplicities of the nonequivalent O sites with the respective bond distances, bond angles, and vacancy formation energies in the dilute limit.

Site	m	$d_{Mn—O}$ (Å)	$\alpha_{Mn—O—Mn}$ (deg)	ΔH_D^{ref} (eV)
Hexagonal				
O1	1	1.88, 1.88	174.3	3.27
O2	2	1.87, 1.89	171.1	3.27
O3	1	1.91, 1.91	82.0	2.33
O4	2	1.89, 1.92	82.1	2.35
Perovskite				
O1	1	1.90, 1.90	180.0	1.87

not be universally expected, as highlighted by the significant variations between different functionals in $SrMnO_3$ (see Sec. III C).

B. Atomic and magnetic structure of $SrMnO_3$

$SrMnO_{3-\delta}$ has an orthorhombic ground state structure (space group $C222_1$, no. 20), which undergoes a second-order phase transition into a hexagonal phase above room temperature (space group $P6_3/mmc$, no. 194) [42]. The hexagonal structure contains MnO_6 octahedra with both face-sharing and corner-sharing connectivity, and the two nonequivalent O sites have Mn—O—Mn bond angles of 90° and 180°. However, it is likely not a polymorph but only a pseudosymmetric phase [42] resulting from dynamic disorder [43]. This conjecture is confirmed by our calculations, where the structural relaxations in the orthorhombic symmetry, illustrated in Fig. 1(a), lower the energy relative to the hexagonal phase and induce subtle distortions of the octahedra. The symmetry breaking results in four nonequivalent O sites, for which the calculated Mn—O bond lengths and Mn—O—Mn bond angles are given in Table I. The site labels follow the crystallographic information file from the Inorganic Crystal Structure Database (no. 157936). The bond angles clearly show the relation to the two O sites in the higher-symmetry average hexagonal structure. The lowest-energy magnetic structure of $SrMnO_3$ in a 20-atom orthorhombic cell (with four Mn atoms) has an antiferromagnetic configuration as shown in Fig. 1(a). This antiferromagnetic configuration is consistent with the magnetic structure deduced from the low-temperature experiments [42] as well as other DFT calculations [44]. Our calculated local magnetic moment of $2.7\mu_B$ is close to the nominal magnetic moment of $3\mu_B$ for high-spin Mn^{4+}. Irrespective of the symmetry breaking due to distortions and magnetic ordering, giving rise to the orthorhombic ground state symmetry, we refer to this structure as hexagonal $SrMnO_3$.
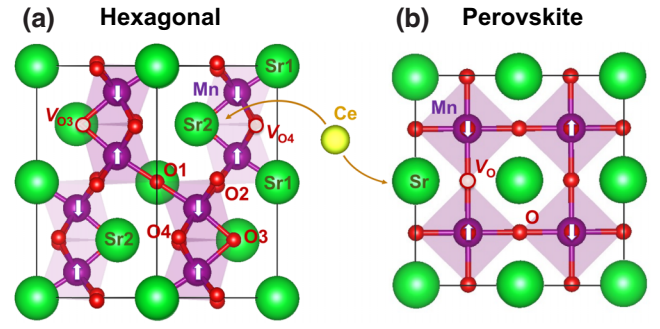
FIG. 1. (a) Hexagonal phase of $SrMnO_3$ in its ground state orthorhombic crystal structure (space group $C222_1$, no. 20) with antiferromagnetic order of Mn spins. The preferred O sites for vacancy formation are indicated. (b) Perovskite phase in its metastable cubic structure ($Pm\bar{3}m$, no. 221). Ce substitutes for Sr to form SCM alloys.

At high temperatures and in the presence of significant O deficiencies ($T > 1400\,°C$, $\delta > 0.25$), $SrMnO_3$ undergoes a phase transition into the cubic perovskite structure [space group $Pm\bar{3}m$, no. 221; Fig. 1(b)], which can also exist as a metastable phase above about $800\,°C$ [45,46]. Since the hexagonal to cubic phase transition occurs within the range of thermodynamic conditions of interest for STCH, we consider both phases. Using crystal structure sampling via kinetically limited minimization [47], we confirmed that the cubic phase is indeed the most stable perovskite structure, not just a pseudosymmetric average structure (see also Sec. III B). This test is important for the subsequent supercell calculations reported below, because energy-lowering lattice distortions could appear as spurious contributions to the defect formation energy. Further, we obtain a G-type antiferromagnetic ordering [44,48], which is also indicated in Fig. 1(b). For the SCAN+U functional, the perovskite structure lies 156 meV per formula unit (f.u.) above the hexagonal phase. The SCAN+U relaxed structures of the hexagonal and perovskite phases are available in Supplemental Material [49] as crystallographic information files generated with the FINDSYM code [50].

C. Reduction of $SrMnO_3$

To describe the reduction of $SrMnO_3$, we start by calculating the V_O defect formation energies in the hexagonal phase using the SCAN+U functional. We broadly follow the approach and terminology in Ref. [51]; additional details are given in Sec. III. Other intrinsic vacancy (V_{Sr1}, V_{Sr2}, V_{Mn}) and interstitial (Sr_i, Mn_i, O_i) defects were also considered but their formation energies were found to be significantly higher under typical STCH reduction and oxidation conditions. The V_O defect formation energies ΔH_D^{ref} for the reference condition (O chemical potential $\Delta\mu_O =$

0) are given in Table I. The charge-neutral vacancies introduce two excess electrons into the system. Because of the relatively high Mn oxidation state, these electrons readily reduce the two Mn neighbor atoms from the 4+ oxidation state to the 3+ oxidation state, which is accompanied by an increase of the local magnetic moment from $2.7\mu_B$ to $3.5\mu_B$. The formation of charged vacancies with itinerant electrons is much less favorable, as evident from the charge transition levels being separated from the conduction band minimum by more than 1.5 eV in SCAN+U calculations. We conclude that for the present system, electronic entropy contributions are not of significant importance. However, we note that in systems that are more susceptible to charge exchange between defects and the bulk, electronic free energy contributions and the temperature dependence of the Fermi level can play an essential role for thermochemical equilibria [22].

As seen in Table I, the O sites with a Mn—O—Mn angle close to 90° have a vacancy formation energy almost 1 eV lower than the sites with an angle close to 180° and are therefore expected to dominate the reduction behavior by a factor of about 1000 or higher for the temperature range of interest. Thus, for simplicity, we consider the vacancies at the O3 and O4 sites as one defect and omit the O1 and O2 defects. The perovskite phase has only one O site, with a vacancy formation energy almost 0.5 eV lower in energy than in the hexagonal phase (Table I). Because of the significant concentration dependence of ΔH_D, we give in Table I the values obtained by extrapolating results obtained with different supercell sizes to the dilute limit (see Sec. III C).

In our thermodynamic modeling approach for defect equilibria [22,27], the concentration c_D of a charge-neutral defect with formation energy ΔH_D follows

$$\frac{c_D}{N_S} = \frac{\exp(-\Delta H_D/k_B T)}{1 + \exp(-\Delta H_D/k_B T)}, \quad (1)$$

where N_S is the density of the lattice sites hosting the defect and k_B is the Boltzmann constant. Importantly, Eq. (1) minimizes the total free energy of defect formation, including the enthalpy contributions ΔH_D from the noninteracting defects and the configurational entropy contribution of a random defect distribution on the respective sublattice. The denominator of Eq. (1) is often omitted in the dilute limit but becomes significant in the case of nondilute concentrations. Considering the multiplicities of the O sites in Table I, we obtain the off-stoichiometry δ from the fractional vacancy site concentration $x_V = c_D/N_S$ ($0 \leq x_V \leq 1$) using factors $f_d = 1.5$ and $f_d = 3.0$ for the hexagonal and perovskite phases, respectively, i.e., $\delta = f_d \times x_V$.

At any given temperature T and partial pressure of O_2, we determine $\Delta\mu_O$ from the ideal gas law (see Sec. III D) to obtain $\Delta H_D = \Delta H_D^{ref} + \Delta\mu_O$. Using the formation energies ΔH_D^{ref} for noninteracting defects from Table I, we
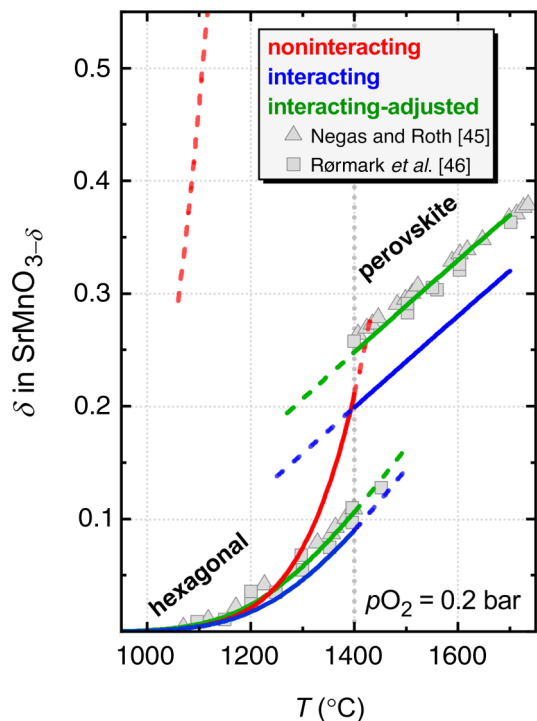
FIG. 2. Thermodynamic defect equilibria as a function of temperature in air ($pO_2 = 0.2$ bar) for the hexagonal and perovskite phases of SrMnO$_{3-\delta}$, obtained from the noninteracting (red), interacting (blue), and interacting-adjusted (green) defect models. Experimental data from the literature are shown by gray symbols. The phase transition occurs at 1400 °C in experiments. The dashed lines show the results for the respective phases beyond the phase transition. The interacting-adjusted model includes a reduction of the $\Delta H_D^{ref}(V_O)$ dilute-limit defect formation energies by 0.05 and 0.18 eV in the hexagonal and perovskite phases, respectively, compared to the SCAN+U-calculated values given in Table I. The interaction parameters a_0 and a_1 in Table III are unchanged.

show the resulting off-stoichiometry of SrMnO$_{3-\delta}$ in air ($pO_2 = 0.2$ bar) in Fig. 2 (red lines) as a function of T. In the hexagonal phase, this model agrees well with the experimental data [14,45,46] up to $\delta \approx 0.05$, but overestimates δ systematically and significantly at higher temperatures and higher off-stoichiometries. For example, close to the hexagonal to perovskite phase transition at 1400°C, the noninteracting model results in $\delta = 0.21$, well above the experimental values of around 0.10. The discrepancy is even more pronounced for the perovskite phase (dashed red line in Fig. 2). Whereas the experimental data indicate a moderate O deficiency δ of about 0.26 under the same (pO_2, T) conditions, the absolute value of the O chemical potential $\Delta\mu_O = -2.08$ eV is now larger than ΔH_D^{ref} for the perovskite phase (see Table I), implying that vacant O sites are more favorable than occupied sites and yielding an unphysical result of $\delta = 2.4$ according to Eq. (1).

D. Incorporating ensemble statistics for interacting defects

Underpinning the simple model considered so far is the assumption that the defects are spatially well separated such that they do not interact with each other and the defect formation energy is independent of the concentration. This assumption is usually justified in the limit of dilute or moderate defect concentrations, but viable STCH materials require a high degree of reduction, where defect interactions are likely to become important. The overestimated vacancy concentrations in the noninteracting model indicate that the defect interactions are repulsive. This situation is fundamentally different from the attractive forces occurring between defects, dopants, and impurities when they have charges of opposite sign [28,29,52–54], e.g., in the case of donor-acceptor pairs, or when they have opposite atomic size mismatches relative to the host atoms [27], which create mutually canceling strain fields. In the case of attractive forces, one can enumerate a limited number of dopant-defect pair and complex configurations, calculate their binding energies, and incorporate them in the defect and charge equilibrium using the law of mass action [27,29,55]. Because of the difficulty to enumerate unbound configurations and to quantify the corresponding entropy

TABLE II. Number of total (tot) and nonequivalent (neq) V_O pair and triplet configurations for different supercell sizes, and the corresponding O deficiency δ.

Supercell (hexagonal)	60	80	240
Pair (tot)	153	276	2556
Pair (neq)	18	26	85
δ	0.167	0.125	0.042
Triplet (tot)	816	2024	. . .
Triplet (neq)	72	144	. . .
δ	0.250	0.188	. . .
Supercell (perovskite)	40	80	160
Pair (tot)	276	1128	4560
Pair (neq)	11	13	15
δ	0.25	0.125	0.063
Triplet (tot)	2024	17 296	. . .
Triplet (neq)	14	140	. . .
δ	0.375	0.188	. . .

contributions, here we use a sampling-based statistical mechanics approach instead.

Figure 3(a) illustrates the present approach for predicting the concentration-dependent energy distribution for interacting defects with different supercell sizes and defect populations. We construct supercells for hexagonal $SnMnO_3$ with 60, 80, and 240 atomic sites and with 40, 80, and 160 sites for the perovskite phase. On the basis of a symmetry analysis, we enumerate all nonequivalent vacancy pair (number of constituents $n = 2$; all supercells) and triplet ($n = 3$; the two smaller cells) configurations with their respective degeneracies g_i, as summarized in Table II (see also Sec. III C). For each nonequivalent configuration i, the interaction energies are calculated as

$$\Delta E_i^{int} = \Delta H_{D,i}(nV_O) - n \times \Delta H_D(V_O), \qquad (2)$$

with use of the extrapolated dilute-limit formation energy $\Delta H_D(V_O)$ as given in Table I, which serves as the reference energy for noninteracting defects.

The approach captures not only the interactions between two (pairs) or three (triplets) defects but also includes the interactions with their periodic images. Thus, it represents an approximation of the full configuration statistics within the periodic boundary conditions of the supercells used. The resulting interaction energies $\Delta E^{int}/n$ per vacancy are shown in Fig. 3(b) for pairs in the hexagonal phase as a function of the pair distance. The interaction energies are about 0.5 eV for close vacancy pairs that share a common Mn neighbor and generally decay with distance. However, $\Delta E^{int}/n$ is not well described by a simple distance-dependent function. In the case of the lower defect concentrations implied by the pairs in the large 240-atom supercell, many configurations exhibit small or negligible interaction energies. In contrast, for smaller supercells (80 and 60 atoms) with pairs and triplets, most

FIG. 3. (a) Interacting defect model using supercells with vacancy pairs and triplets in supercells of different size. (b) Interaction energy $\Delta E^{int}/n$ per vacancy in hexagonal $SrMnO_3$ obtained from supercell calculations of vacancy pairs ($n = 2$) as a function of the pair distance for the three different cell sizes.
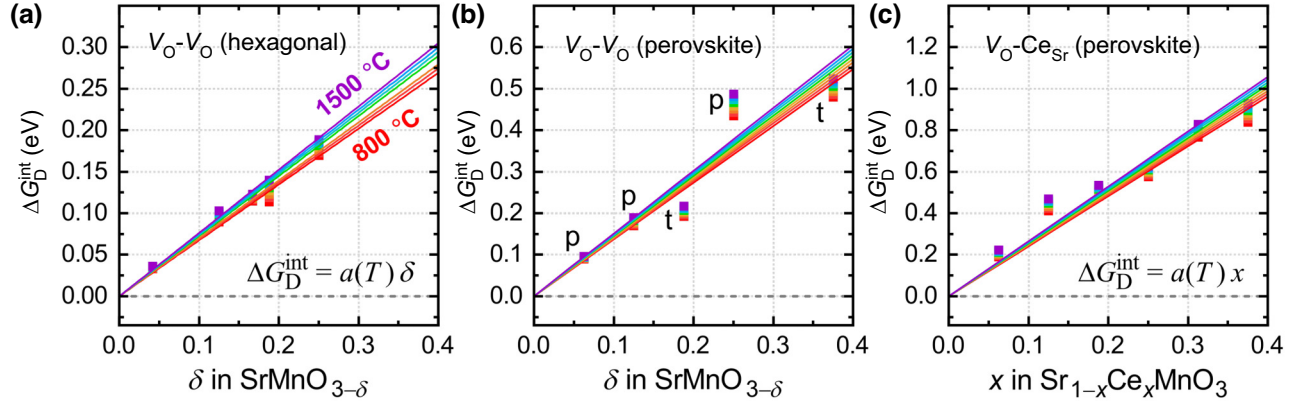
FIG. 4. Temperature-dependent free energy of defect interaction $\Delta G_D^{int}(T)$ for O vacancy formation. The data points show $\Delta G_D^{int}(T)$ as obtained from the supercell sampling [Eq. (3)] and the lines show the parameterization according to Eq. (4) and Table III. (a) V_O-V_O interactions as a function of δ in hexagonal SrMnO$_{3-\delta}$. (b) V_O-V_O interactions as a function of δ in perovskite SrMnO$_{3-\delta}$. "p" and "t" indicate pair and triplet configurations. (c) V_O-Ce$_{Sr}$ interactions as a function of x in the perovskite phase of Sr$_{1-x}$Ce$_x$MnO$_3$.

of the configurations result in $\Delta E^{int}/n \geq 0.05$ eV, signifying that the repulsive interactions become more prominent at higher vacancy concentrations.

To incorporate the statistical supercell energies into a thermodynamic model, we need to consider the effect of the defect interactions on both the enthalpy and the (configurational) entropy. Thus, using normalized degeneracies ($\Sigma g_i = 1$), we determine the temperature-dependent *free* energy of defect interaction as

$$\Delta G_D^{int} = -\frac{k_B T}{n} \ln \sum_i \left(g_i \exp \left(-\Delta E_i^{int}/k_B T \right) \right) \quad (3)$$

for each of the five cases given in Table II (separately). Here, the sum on the right-hand side is the partition function Z^{int} for the interactions in the supercells containing n defects. The approach of calculating pair and triplet configurations for different cell sizes yields ΔG_D^{int} for only certain values of the off-stoichiometry δ. To include the interactions in the thermodynamic simulation, it is desirable to parameterize ΔG_D^{int}. As shown in Figs. 4(a) and 4(b), the free energy of defect interaction can be expressed to a good approximation as a linear function in T and δ within the interval $800\,°C \leq T \leq 1500\,°C$:

$$\Delta G_D^{int}(T) = (a_0 + a_1 T)\delta. \quad (4)$$

The parameters a_0 and a_1, as well as the uncertainty resulting from the fits shown in Fig. 4, are given in Table III.

To determine the concentrations of interacting defects, we consider the total free energy of reduction (i.e., defect formation) ΔG^{tot} per formula unit of SrMnO$_{3-\delta}$. The expression is analogous to the expression in the case of noninteracting defects [56], except that the interaction free energy ΔG_D^{int} per vacancy is now added to the defect formation energy ΔH_D, i.e.,

$$\Delta G^{tot} = f_d \left(x_V \left(\Delta H_D + \Delta G_D^{int} \right) \right.$$
$$\left. + k_B T \left(x_V \ln(x_V) + (1 - x_V) \ln(1 - x_V) \right) \right). \quad (5)$$

Here, we used the fractional vacancy site concentration $x_V = \delta/f_d$ to express the configurational entropy of noninteracting (randomly distributed) lattice defects, and the energies with subscript "D" enter with a proportionality in x_V. The equilibrium concentrations are determined by the free energy minimum condition $d\Delta G^{tot}/dx_V = 0$, which, in the absence of defect interactions, yields Eq. (1). Including the free energy contribution due to defect interactions results in an additional term $d(x_V \Delta G_D^{int})/dx_V = 2(a_0 + a_1 T)f_d x_V$ within the parameterization of Eq. (4) [note the factor 2 resulting from the x_V dependence in both Eq. (4) and Eq. (5)]. Since this concentration-dependent term adds to the defect formation energy ΔH_D on the right-hand side

TABLE III. Parameterization of $\Delta G_D^{int}(T)$ according to Eq. (4) for SrMnO$_{3-\delta}$ and an analogous expression proportional to x in Sr$_{1-x}$Ce$_x$MnO$_3$. The last column gives the average uncertainty of the resulting $a(T)$ over the temperature window between 800 and 1500 °C.

Interaction	Phase	Proportionality	a_0 (eV)	a_1 (10^{-3} eV/K)	Average uncertainty (eV)
V_O-V_O	Hexagonal	δ	0.54	0.13	±0.02
V_O-V_O	Perovskite	δ	1.15	0.21	±0.12
V_O-Ce$_{Sr}$	Perovskite	x	2.04	0.34	±0.12

of Eq. (1), we use a self-consistency condition to solve for the equilibrium concentrations. The resulting free energy gain ΔG^{tot} due to O vacancy formation, per formula unit, is then given directly by Eq. (5).

For further analysis, we separate $\Delta G^{\text{tot}} = \Delta H^{\text{red}} - T\Delta S^{\text{red}} + \delta\Delta\mu_O$ into enthalpy and entropy contributions (per formula unit) and calculate $(\partial/\partial\delta)\Delta S^{\text{red}} = (\partial/\partial T)\Delta\mu_O$ [22] for the differential reduction entropy (per removed O atom, using the shorthand notation δS^{red} for the remainder of this article). In Sec. II G, we discuss specific results in SCM alloys for the differential and absolute reduction entropies. As reflected by the positive values of a_1 in Table III, the inclusion of ΔG_D^{int} implies a negative entropy of defect interaction, which can be understood by considering that the noninteracting system already includes the maximum configurational entropy of the random defect distribution [see Eq. (5)]. Thus, the correlations introduced by defect interactions reduce the entropy relative to the noninteracting case, but the total entropy of defect formation ΔS^{red} remains positive. Further, while the linear model for $\Delta G_D^{\text{int}} = \Delta H_D^{\text{int}} - T\Delta S_D^{\text{int}}$ (Eq. (4)) provides accurate reduction properties for the present system under the range of conditions considered, it implies—by construction—a temperature-independent interaction enthalpy and entropy. This is a reasonable approximation only within a finite temperature interval (here, $800\,°C \leq T \leq 1500\,°C$), but consider, for example, that $\Delta S_D^{\text{int}} \to 0$ in the infinite temperature limit, so to recover the entropy of the random defect distribution (*cf.* Eq. (5)). If needed or desired, the expansion of Eq. (4) to higher orders in T is straightforward (2$^{\text{nd}}$ order coefficients are also included in the Supplemental Material [49]).

Recalculating the equilibria for SrMnO$_{3-\delta}$ with defect interactions (blue lines in Fig. 2) yields very good agreement with experiment in the hexagonal phase up to the phase transition temperature. In the perovskite phase, the predicted $\delta = 0.20$ is reasonably close to the experimental value of 0.26 at $1400\,°C$, and increases at a similar rate as the experimental data. Thus, even though the interaction energies of around 0.3 eV at these concentrations [see Fig. 4(b)] are modest compared to the absolute formation energies at the reference condition (Table I), they are nevertheless essential for achieving an even qualitatively meaningful description of defect equilibria under strongly off-stoichiometric conditions when compared with the noninteracting model (Fig. 2, red lines). Further, as illustrated in Fig. 2 (green lines), it takes an adjustment of the dilute-limit ΔH_D^{ref} by only -0.05 and -0.18 eV (without changing the interaction parameters) in the hexagonal and perovskite phases, respectively, to bring the simulated data into full agreement with the experimental data. This level of agreement speaks to the accuracy of the SCAN+U functional for the present material system, considering the variation of formation energies between different total

energy functionals (see Sec. III C). It is also remarkable that the interacting defect model correctly describes the temperature dependence up to $1700\,°C$, even though we do not explicitly consider vibrational effects. It is worth noting that vibrational free energy contributions were found to be not significant for O vacancy formation in hercynite spinels [20], although the generality of this finding is an open question.

The free energy of reduction, resulting from O vacancy defect formation, can play a critical role in the temperature- and $p O_2$-dependent phase transitions, as recently demonstrated in barium manganates [56] within a noninteracting defect model. To address the role of oxygen defect formation in the hexagonal-perovskite phase transition of SrMnO$_3$, we evaluate the total free energy of reduction ΔG^{tot} [Eq. (5)] at the phase transition conditions ($T = 1400\,°C$, $p O_2 = 0.2$ bar). We obtain a free energy gain of 20 and 89 meV/f.u. for the hexagonal and perovskite phases, respectively, showing that defect formation stabilizes the perovskite phase, although the relative gain is not sufficient to overcome the low-temperature energy preference of 156 meV/f.u. in favor of the hexagonal phase in SCAN+U calculations. However, the gains in ΔG^{tot} increase to 25 and 129 meV/f.u. when we use the adjusted dilute-limit defect formation energies (see Fig. 2, green lines). Considering the substantial variations in the 0-K phase stability energies between different functionals (see Sec. III C), the present results are consistent with the assumption that the phase transition is primarily driven by the defect formation. A more definitive assessment would require calculations of the polymorphic energy ordering beyond the DFT level, e.g., as in Ref. [38], as well as quantification of vibrational free energy contributions, including zero-point energies (ZPEs). These are interesting issues for future studies, but the details of the phase transition behavior are not of central concern for the present study. For the simulation of the water splitting redox processes in this section, we use the unadjusted, first-principles-calculated defect energies and interaction parameters.

E. Sr$_{1-x}$Ce$_x$MnO$_{3-\delta}$ alloy calculations

In contrast to the line compound Ba$_4$CeMn$_3$O$_{12}$, where Ce partially replaces (compositionally if not structurally) Mn in BaMnO$_3$ [8,57], Ce substitutes for the *A*-site element Sr in SrMnO$_3$ to form a solid solution [14,58,59]. To compare this experimental observation with our computational predictions, we show in Table IV the formation energies ΔH_D for Ce substitution at both the Mn sites and the Sr sites. The relevant formation energies under equilibrium conditions depend on the specific values of the chemical potentials $\Delta\mu$ for Ce, Sr, and Mn. To obtain representative values under conditions relevant for the present

TABLE IV. Calculated defect formation energies for Ce substitution at the Sr and Mn sites in the hexagonal and perovskite phases of SrMnO$_3$. ΔH_D^{ref} gives the value for the elemental reference condition ($\Delta\mu = 0$). For representative reducing conditions, we give ΔH_D at $\Delta\mu = -2.10, -7.12, -4.40$, and -2.00 eV, for O, Ce, Sr, and Mn, respectively.

Phase	Defect type	ΔH_D^{ref} (eV)	ΔH_D (eV)
Hexagonal	Ce$_{Sr1}$	-1.39	1.33
	Ce$_{Sr2}$	-1.62	1.10
	Ce$_{Mn}$	-1.91	3.21
Perovskite	Ce$_{Sr}$	-2.95	-0.22
	Ce$_{Mn}$	-3.06	2.07

work, we constructed the phase diagram from the formation enthalpies ΔH_f of all phases in the Sr-Mn-O space, as shown in Fig. S1 in Supplemental Material [49]. The chemical potentials given in the caption for Table IV correspond to the stability limit of the hexagonal phase under reducing conditions in that diagram ($\Delta\mu_O = -2.10$ eV), while $\Delta\mu_{Ce}$ is determined by the coexistence condition with CeO$_2$. We see in Table IV that Ce strongly prefers substitution for Sr over substitution for Mn in both phases under these conditions, with a moderate preference for Sr2 over Sr1 in the hexagonal phase. Notably, the formation energy of Ce$_{Sr}$ in the perovskite phase is negative. For stable phases, negative defect formation energies generally indicate the existence of competing phases, which would limit the chemical potentials such that ΔH_D becomes positive. However, here the negative energy is a consequence of the low-temperature metastable character of the perovskite phase. We briefly revisit this issue below in the context of alloy mixing enthalpies.

To model the SCM alloys, we use the special quasirandom structure (SQS) approach [60], which provides good representations of random alloys in relatively small simulation cells. For hexagonal SrMnO$_3$, we use SQS alloy models with Ce only at Sr2 sites, which show consistently lower energies than mixed configurations, as expected from the substitution energies (Table IV). We choose three different SQS configurations for each Ce content x and find only a small variation of within 2–5 meV/atom between different configurations. The lowest-energy SQS structures for each Ce content were selected for the following studies and are available in Supplemental Material [49].

In the Ce-rich limit ($x = 1$), one could expect the formation of CeMnO$_3$, which, however, is not known. We performed crystal structure prediction for such a hypothetical compound using the approach in Ref. [47], but found no structure that would be stable against decomposition into CeO$_2$ and MnO. Thus, we calculate the mixing enthalpy of SCM as

$$\Delta H_{mix} = E_{SCM} - (1 - x)E_{SrMnO_3} - x(E_{CeO_2} + E_{MnO}),$$
(6)
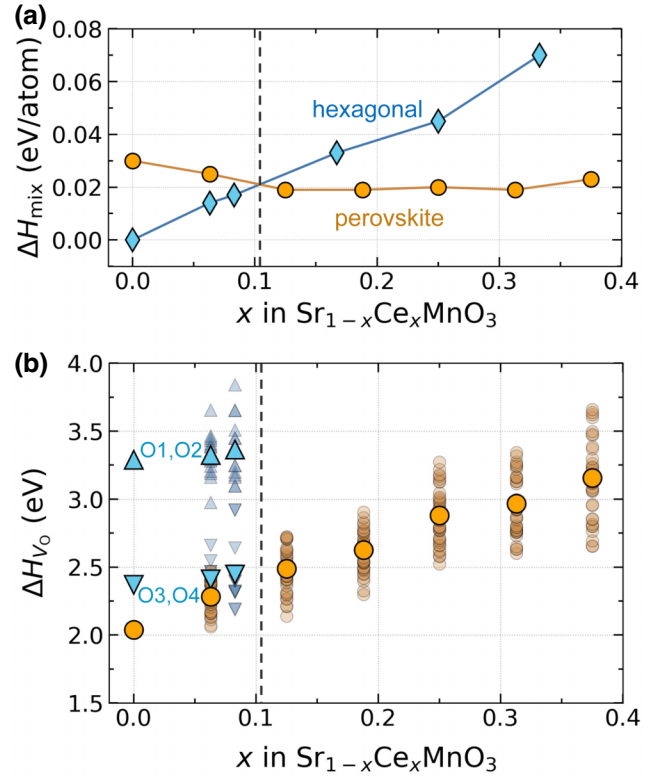
FIG. 5. (a) Enthalpy of mixing ΔH_{mix} of SCM alloys in the hexagonal and perovskite phases, showing a phase transition around $x = 0.1$. (b) Distribution of oxygen vacancy formation energies in the SCM alloys as a function of the Ce concentration. The hexagonal phase has two groups of O sites with similar formation energies, whereas the perovskite phase has only a single O site. The data points with the larger symbol size show the average formation energies.

shown in Fig. 5(a). The ΔH_{mix} values of the two phases intersect at around $x = 0.10$, above which the perovskite phase becomes more stable than the hexagonal phase. The calculated critical Ce content is about twice as large as the experimentally observed transition composition at $x = 0.05$ [61]. This discrepancy could indicate that the SCAN+U functional overestimates the energy difference between the two phases, which would also affect the temperature-dependent phase transition, as discussed above. Further, we observe that ΔH_{mix} in the perovskite phase initially (i.e., close to $x = 0$) slopes downward, corresponding to the negative defect formation energy of Ce$_{Sr}$ in this phase (see Table IV). Negative defect formation energies usually indicate an instability against an ordered stoichiometric phase. Here, however, such an instability is superseded by the instability against the hexagonal phase at low Ce contents [see Fig. 5(a)], which has positive formation energies for Ce substitution. The mixing enthalpies ΔH_{mix} assume small, positive values over the composition range considered, which is consistent with the formation of a solid solution.

Figure 5(b) shows the distribution of O vacancy formation energies as a function of the Ce content. On the basis of this distribution, we determine the free energy of defect interaction ΔG_D^{int} for V_O-Ce$_{Sr}$ interactions, as shown in Fig. 4(c), in a fashion analogous to that used for the V_O-V_O interactions discussed above. However, the configuration sampling is now simpler than in the case of the vacancy interactions, as it consists merely in evaluating the defect energies for all individual O sites in the SQS structures. The interaction energies ΔE_i^{int} [see Eq. (2)] are evaluated with $n = 1$ relative to ΔH_D in SrMnO$_3$ without Ce alloying, and we have $g_i = 1$ in Eq. (3) since the O sites are all inequivalent in the low-symmetry SQS structures. We further note that for the case of defect interactions with extrinsic dopants (here Ce alloy substitutions), the present approach becomes identical to the concept of the "effective formation energy" [30], which is a weighted-average formation energy resulting in the same defect concentration as the sum over all nonequivalent sites. Furthermore, we determine a parameterization analogous to Eq. (4), but with a proportionality in the Ce content x instead of δ, with the values of the parameters given in Table III. The respective additional term in the vacancy concentration $x_V = \delta/f_d$, Eq. (1), is obtained as $d(x_V \Delta G_D^{int})/dx_V = (a_0 + a_1 T)x$ (without the factor 2 from the V_O-V_O case, because the V_O-Ce$_{Sr}$ interaction is proportional only to x, not to x_V).

F. Modeling of water splitting with SCM

In the following thermodynamic modeling, we use a superposition principle for the V_O-Ce$_{Sr}$ and V_O-V_O interactions to determine $\Delta G_D^{int}(\delta, x, T)$ for continuous values of δ, x, and T, using again a self-consistency criterion for δ in Eqs. (1) and (4). Given that even low levels of Ce substitution, as well as lower than ambient O$_2$ partial pressures (see Fig. 2) tend to stabilize the perovskite phase over the hexagonal phase, we consider only the former for simulating the reduction and oxidation processes at temperatures above 800 °C. Figure 6(a) shows the off-stoichiometry δ_{red} of perovskite SCM as a function of x and T_{red} during reduction at $pO_2 = 10^{-4}$ bar. The data are in good overall agreement with experimental results from thermogravimetric analysis [14], and we include analogous data from the experimental analysis [14] in Supplemental Material (Fig. S2) [49] for comparison. As for the Ce content dependence, we obtain $\delta_{red} = 0.35$ at $T_{red} = 1400$ °C for $x = 0$, where the larger off-stoichiometry reflects the lower O$_2$ partial pressure compared with the O$_2$ partial pressure for Fig. 2. As a result of the repulsive V_O-Ce$_{Sr}$ interactions [see Fig. 4(c)], the vacancy concentration decreases to $\delta_{red} = 0.08$ at $x = 0.4$ (see also Table V).

For the oxidation step during which H$_2$ is released, we take $T_{ox} = 850$ °C and $pH_2O = 1$ bar. The amount of H$_2$ produced is proportional to the change in δ relative to the
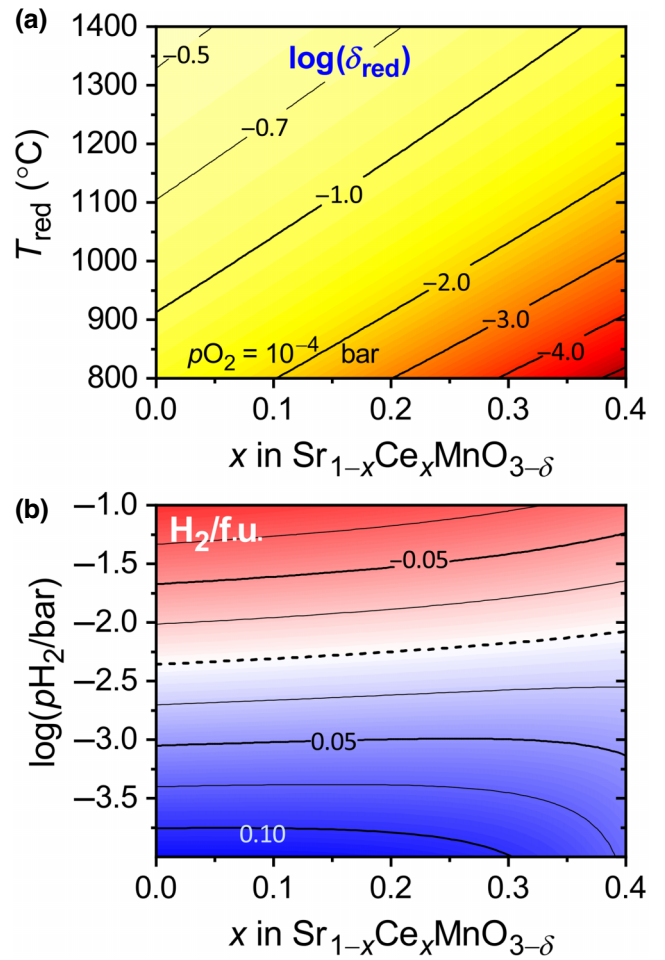
FIG. 6. (a) Off-stoichiometry $\log(\delta_{red})$ in Sr$_{1-x}$Ce$_x$MnO$_{3-\delta}$ in the perovskite phase as a function of Ce content x and temperature T_{red} during reduction at $pO_2 = 10^{-4}$ bar. Note that $\log(\delta) = -0.7$ and $\log(\delta) = -0.5$ correspond approximately to $\delta = 0.2$ and $\delta = 0.3$, respectively. (b) Hydrogen production in number of H$_2$ molecules per SCM formula unit, shown as a function of x and the H$_2$ partial pressure in $\log(pH_2/\text{bar})$. The underlying process conditions are $T_{red} = 1400$ °C and $pO_2 = 10^{-4}$ bar for the reduction step and $T_{ox} = 850$ °C and $pH_2O = 1$ bar for the oxidation step. Note that pH_2/bar corresponds to the H$_2$:H$_2$O ratio. The dashed line (H$_2$/f.u. = 0) represents the demarcation line at which net water splitting (H$_2$/f.u. > 0) occurs.

reduction step, which in turn depends on pO_2 and the corresponding O chemical potential during the oxidation step. We use the H$_2$O $\longleftrightarrow$ H$_2$ + $\frac{1}{2}$O$_2$ equilibrium and the ideal gas law to determine the dependence of $\Delta\mu_O$ on pH_2 (see Sec. III D). As a result of this relationship, the H$_2$ production generally decreases with increasing H$_2$ partial pressure and the corresponding H$_2$:H$_2$O ratio.

Figure 6(b) shows the resulting water splitting yield H$_2$/f.u. = $\delta_{red} - \delta_{ox}$ (number of H$_2$ molecules per SCM formula unit) as a function of Ce content x and pH_2. We observe a strong dependence on the H$_2$:H$_2$O ratio, with a critical pH_2 for net water splitting below 10^{-2} bar.

TABLE V. Entropy analysis of the SCM water splitting redox process. Given are, as a function of the Ce content x, the O off-stoichiometry $\delta = \delta_{red} = \delta_{ox}$, pH_2 [see Fig. 6(b), dashed line], and the differential reduction entropies for the present interacting defect model (δS^{red}) and for a hypothetical noninteracting system (δS_{ni}^{red}) for the same δ.

x	δ	$\log(pH_2/bar)$	δS^{red} (k_B per O atom)	δS_{ni}^{red} (k_B per O atom)
0.0	0.35	−2.36	0.33	2.02
0.1	0.28	−2.31	0.56	2.28
0.2	0.21	−2.25	0.84	2.61
0.3	0.14	−2.18	1.18	3.03
0.4	0.08	−2.08	1.66	3.61

This behavior is almost universal in STCH materials with the notable exception of CeO$_2$, which can split water at higher pH_2 [8,9]. Increasing the Ce content can increase pH_2, as seen in the upward trend of the threshold for net water splitting [dashed line in Fig. 6(b)], increasing from $\log(pH_2/bar) = -2.4$ at $x = 0$ to $\log(pH_2/bar) = -2.1$ at $x = 0.4$. However, significant H$_2$ production, e.g., H$_2$/f.u. = 0.05 requires a lower H$_2$:H$_2$O ratio, which barely changes with Ce content up to $x = 0.3$ and even drops at higher x values [Fig. 6(b)]. The insensitivity of net H$_2$ production results from a similar x dependence of δ_{red} and δ_{ox}, and the insufficient amount of initial reduction [see Fig. 6(a)] at high Ce content causes the corresponding drop in H$_2$ production. The difficulty to increase the H$_2$:H$_2$O ratio by Ce alloying without sacrificing H$_2$ yield is related to the effect on the reduction entropy (see below). Overall, our simulation data shown in Fig. 6 provide not only a qualitative but also a near-quantitative model based on first-principles calculations, explaining recent experimental observations [14].

G. Analysis of the reduction entropy

The thermodynamic modeling further allows us to analyze the solid state entropy and to relate it to the water splitting performance. At the critical pH_2 [dashed line in Fig. 6(b)], we have a constant stoichiometry ($\delta_{ox} = \delta_{red}$), so the differential reduction entropy δS^{red} (shorthand as defined above), given in Table V, corresponds to the change of the O chemical potential over the temperature difference $T_{red} - T_{ox} = 550$ K [22]. Relative to the hypothetical noninteracting ideal solution system at the same O stoichiometry, the differential entropy is strongly suppressed. Interestingly, δS^{red} can even become negative, e.g., above $\delta = 0.4$ in pure SrMnO$_3$, whereas this happens in the hypothetical noninteracting system only at much higher off-stoichiometries, i.e., above half occupancy ($\delta > 1.5$). Despite the strong reduction of δS^{red} (see Table V), the (always positive) absolute reduction entropies ΔS^{red} per formula unit are still comparable to

the absolute reduction entropies for the ideal solution. For example, at $x = 0$ and $\delta = 0.35$, we obtain $\Delta S^{red} = 6.8 \times 10^{-5}$ eV/K per formula unit for the interacting system, compared to 9.4×10^{-5} eV/K per formula unit for the hypothetical noninteracting system.

The primary significance of the entropy analysis lies in the relation between the differential reduction entropy and the H$_2$:H$_2$O ratio. Since δS^{red} corresponds to the temperature dependence of the O chemical potential [22], a higher entropy implies a lower $\Delta\mu_O$ at the lower oxidation temperature, which translates into a higher pH_2 according to the water gas phase equilibrium. This relationship is also borne out in Table V, where pH_2 at the water splitting threshold (zero yield) condition increases with δS_{int}^{red} and the Ce content, but at the expense of a lower O deficiency, which limits the potential yield at lower pH_2. The reduction of δS^{red} compared to the ideal solution behavior illustrates how repulsive defect interactions exacerbate the problem that higher total H$_2$ yields generally necessitate lower H$_2$:H$_2$O ratios. A similar drawback results from attractive defect interactions [20], reflecting the fact that the configurational entropy is maximized for random defect distributions and is lowered in the case of either attractive or repulsive interactions. Thus, the optimal design strategy for elemental substitutions (alloying) should aim to minimize defect interactions, ideally maintaining all defect formation energies in a narrow range for all O sites.

Even so, the entropy δS^{red} necessary to achieve desirable H$_2$:H$_2$O ratios on the order of 1:10 is around $10 k_B$ per O atom [22], which is considerably higher than the configurational entropies resulting from a conventional charge-neutral defect mechanism, especially in the presence of defect interactions (see Table V). Thus, overcoming the unfavorable trade-off between H$_2$ yields and hydrogen-steam ratios will likely require the use of additional sources of entropy, such as electronic entropies due to charged defect formation [22] or partially occupied lanthanide f orbitals [62]. These effects could be at work in CeO$_2$, which is known to have a higher reduction entropy than other oxides, especially at low defect concentrations [63]. A better understanding of the physical mechanisms involved in the reduction of CeO$_2$ could provide important insights into the design of novel STCH oxides. However, we caution that a quantitative assessment of the Fermi level–dependent charge exchange between defects and the bulk likely requires a quasiparticle energy (band gap)–corrected approach beyond DFT (see also Sec. III C).

III. COMPUTATIONAL METHODS

A. First-principles calculations

Total energy and defect calculations were performed with use of the projector augmented wave (PAW) method [64,65] as implemented in Vienna Ab initio Simulation

Package (VASP) [66]. We used three different approximations for exchange and correlation effects to gauge the sensitivity of the O vacancy formation energy on the level of theory: (1) The generalized gradient approximation (GGA) [67], (2) the meta-GGA SCAN functional [40], and (3) the HSE06 hybrid functional [68,69] with conventional settings (25% Fock exchange and 0.2 Å^{-1} for the range separation parameter). The PAW potentials "Sr_sv", "O_s", "Mn," and "Ce_h" were used with a plane wave energy cutoff of 350 eV or higher, in consistency with the computational approach used in previous studies on transition metal oxides [20,47,51,70]. For SCAN calculations, we used PAW dataset version 5.4 distributed with VASP. With GGA and SCAN functionals, we further used the DFT+U [41] approach. For GGA+U calculations, we use $U_d = 3.0$ eV for the $3d$ transition metals up to Ni [70], as well as $U_d = 1.5$ eV and $U_f = 2.0$ eV for Ce [47]. For SCAN+U calculations, we determined $U_d = 2.0$ eV for Mn, Fe, and Co from the relative stability of oxides with different oxidation states (see Fig. S3) [49], which is comparable to previous literature results [71]. Similarly, we determined $U_f = 1.0$ eV ($U_d = 0$) for Ce for the SCAN functional.

The prediction of compound formation enthalpies ΔH_f (see Table S1 and Fig. S1) [49] and of absolute defect formation energies requires elemental reference energies μ^{ref}. Standard DFT functionals such as the GGA functional exhibit systematic deviations of ΔH_f due to inconsistencies between compound and elemental energies [72], which we corrected by using the fitted elemental reference energies (FERE) [70]. The HSE06 functional shows similar deviations, and FEREs were determined before for select elements [20,51], including oxygen, which is used here. For compatibility with the previously determined "O_s" FEREs for the GGA [70] and HSE06 (supporting information for Ref. [20]) functionals, we used PAW dataset version 4.6 for these functionals. The SCAN functional does not exhibit such systematic errors [73], but for elements treated with the DFT+U formalism, it is still necessary to determine the FERE, because a single U parameter generally does not simultaneously describe

TABLE VI. Elemental reference energies μ^{ref} for SCAN calculations, specifying the PAW dataset (VASP version 5.4 distribution) and the method of calculation. For elements calculated with the SCAN+U functional, the value of U and the respective angular momentum l are given.

Element	PAW potential	Method	U (eV) (l)	μ^{ref} (eV)
O	O_s[a]	SCAN	. . .	−6.18
Sr	Sr_sv	SCAN	. . .	−22.27
Mn	Mn	FERE	2.0 (d)	−17.77
Ce	Ce_h	FERE	1.0 (f)	−44.36

[a] O$_2$ binding energy calculated with "O_h."

well both the compound and the elemental metal [51]. Table VI summarizes the elemental reference energies used for SCAN(+U) calculations. The FEREs for Mn and Ce were determined with experimental compound formation enthalpies ΔH_f of MnO, MnO$_2$, Mn$_3$O$_4$, Mn$_2$O$_3$, CeO$_2$, and Ce$_2$O$_3$ [74]. In the present approach, the calculated ΔH_f values agree with experimental values (where known) to within 0.06 eV/atom in the Sr-Mn-Ce oxide space [74–76]. In addition to total energy calculations, we also performed electronic structure calculations in the GW approximation [77,78], using specifications consistent with the National Renewable Energy Laboratory materials database [79–81], so to compare the predicted band gaps (see below).

Irrespective of the choice of the DFT functional, PAW calculations of molecules with small interatomic distances, such as O$_2$, necessitate the use of "hard" pseudopotentials to avoid spurious energy and force contributions originating from the overlap of pseudization spheres [51]. To circumvent the excess computational load of performing all calculations at the high 910-eV energy cutoff required for the "O_h" PAW potential, we used a two-step procedure to determine the elemental reference energy $\mu_{\text{O}}^{\text{ref}}$ for oxygen in SCAN calculations: First, using "O_h," we calculated the O$_2$ binding energy $E_b^h = E^h(\text{O}_2) - 2E^h(\text{O})$. Here, both the O$_2$ molecule and the O atom are spin-polarized, and for the O atom, we used the symmetry-broken ground state with integer occupations (see Ref. [20] and corresponding supporting information for further details). Second, we obtained the elemental reference energy by adding half the binding energy to the corresponding energy of the free O atom calculated with "O_s," i.e., $\mu_{\text{O}}^{\text{ref}} = E^s(\text{O}) + \frac{1}{2}E_b^h$. Further, we added in Table VI the experimental ZPE of 0.049 eV/O [82] to $\mu_{\text{O}}^{\text{ref}}$, which is expected to outweigh the ZPE contributions in the solid state (for GGA and HSE06 calculations, the ZPE contribution is included in the respective FERE [72]).

B. Structure prediction calculations

Using the kinetically limited minimization approach described in Ref. [47], we performed unconstrained structure sampling for SrMnO$_3$ and CeMnO$_3$ for cell sizes of 10 and 20 atoms. For computational efficiency, this crystal structure search was performed at the GGA+U level. Crystal structure symmetry analysis was performed with the FINDSYM code [50]. For SrMnO$_3$, the motivation was to determine whether the experimentally known cubic perovskite phase is a true polymorph or a pseudosymmetric high-temperature phase. In the latter case, the structure prediction should identify a lower-energy distorted perovskite structure that could be difficult to observe experimentally because of the phase transition to the hexagonal (nonperovskite) structure at lower temperatures. The overall lowest-energy structure identified by the search was a

variant of hexagonal $SrMnO_3$ with a 20-atom primitive cell and practically identical energy (within 0.1 meV/atom) as the orthorhombic structure discussed above. The most favorable perovskite structure (ten-atom primitive cell in space group $R\bar{3}c$, no. 167) showed significant distortions but with a relatively small energy gain of 1.5 meV/atom compared to the cubic phase. However, in subsequent SCAN+U calculations, as well as in HSE06 calculations, the distortion was unstable and did not result in an energy gain. We therefore conclude that the cubic perovskite phase of $SrMnO_3$ is a true polymorph. In contrast, in many other cases, notably including the related $CaMnO_3$ [83], the high-temperature phase is dynamically disordered, and the cubic symmetry appears only in the average structure [43].

For $CeMnO_3$, the motivation for structure prediction was the identification of the appropriate end point at $x = 1$ in the mixing enthalpy of the $Sr_{1-x}Ce_xMnO_3$ alloy (Fig. 5). However, the lowest-energy structure identified was still unstable relative to $CeO_2 + MnO$ by a relatively large margin of more than 250 meV/f.u., which is consistent with the fact that no $CeMnO_3$ ternary oxide structure has been reported so far.

C. Supercell calculations

We constructed supercells of the hexagonal and perovskite $SrMnO_3$ phases with sizes between 40 and 270 atoms. The supercell geometries were chosen to keep the distances between the periodic images as large as possible for a given cell volume. We used our automated defects framework [84] to facilitate supercell construction and defect calculations, including the selection of interstitial sites for the initial survey of relevant defects (which was done at the GGA+U level). Following standard procedures for supercell defect calculations, we included atomic force relaxation for all atoms in the supercell (tolerance 0.02 eV/Å) and we kept the cell external parameters fixed. To obtain very accurate formation energies for the dilute limit (Table I), we extrapolated the SCAN+U results from cell sizes of 80 atoms and larger as a linear function of the reciprocal cell volume, resulting in differences of up to 0.18 eV relative to the 80-atom-cell results (see Table VII; a graphical representation of the extrapolation is given in Fig. S4) [49].

To enumerate the nonequivalent configurations of defect pairs and triplets in the supercells (see Table II), we arranged them in groups within which the defects have identical distances. In doing so, we used a tolerance of 10^{-4} Å, considered the periodic images, and determined the degeneracies $g_i = n_i / \sum_i n_i$, where n_i are the numbers of defect pair/triplet configurations within each group. Further, we generated the SQS structures for the SCM alloys using the mcsqs code implemented in the Alloy Theoretic Automated Toolkit [85], using 60- and 80-atom supercells.

For comparison of defect formation energies between different functionals, we used 80-atom cells (without extrapolation); the results are summarized in Table VII. In the case of the perovskite phase, we used the cubic structure for SCAN+U and HSE06 calculations, but for GGA+U calculations, we used the distorted rhombohedral structure (see the preceding subsection). To assess the relative performance of the functionals, we consider that in GGA+U calculations, the ΔH_D^{ref} values for O vacancies are about 0.5–0.6 eV lower than in SCAN+U calculations, and the HSE06 numbers are even lower. We note that the discrepancy would be even larger without the FERE correction to $\Delta\mu_O^{ref}$, which adds about 0.3 eV to ΔH_D^{ref} in both GGA+U and HSE06 calculations [20,51].

Considering that the SCAN+U results seem to overestimate the formation energies by less than 0.2 eV (see Sec. II D), the GGA+U and HSE06 results would result in significantly overestimated O off-stoichiometries and worse agreement with experiment than the SCAN+U results. We further give in Table VII the energy difference $\Delta E_{P\text{-}H}$ between the two $SrMnO_3$ phases for the three functionals. As discussed above, the perovskite-hexagonal energy difference in SCAN+U calculations is already somewhat larger than what can be accounted for by the free energy gain due to reduction at the phase transition conditions. The GGA+U and HSE06 functionals give even larger differences, likely representing substantially overestimated $\Delta E_{P\text{-}H}$ values. We conclude that the SCAN+U functional currently provides the best total energy description of $SrMnO_3$.

However, in systems with charge exchange between defects and the bulk (in the form of either band electrons or small polarons), the defect equilibrium becomes dependent on the position of the Fermi level, which is constrained by the band gap. In this situation, the ability of the total energy functional to also correctly describe the electronic structure becomes more important. Comparing the single-particle energy gaps of the different functionals with GW quasiparticle energy gaps, we find that the SCAN+U functional

TABLE VII. Comparison of predicted formation energies ΔH_D^{ref} (eV) of V_O defects in $SrMnO_3$ in 80-atom supercells and the perovskite-hexagonal energy difference $\Delta E_{P\text{-}H}$ (meV/f.u.) calculated with the different functionals considered in this work. Additionally, the respective single-particle band gaps (generalized Kohn-Sham gaps) in electronvolts are given in comparison with the quasiparticle energy gaps in the GW approximation.

Site	Phase	GGA+U	HSE06	SCAN+U	GW
O1, O2	Hexagonal	2.69	2.45	3.33	
O3, O4	Hexagonal	1.88	1.57	2.40	
O1	Perovskite	1.45	1.16	2.05	
$\Delta E_{P\text{-}H}$		256	239	156	
E_g	Hexagonal	1.84	3.42	2.37	3.51
	Perovskite	0.34	1.73	0.86	1.62

TABLE VIII. Thermochemical gas phase properties for O_2, H_2, and H_2O used in the present work: standard enthalpies H° and entropies S° [74] as well as the ideal-gas constant-pressure heat capacities c_p.

	H° (kJ/mol)	S° (J/mol K)	c_p (k_B)
O_2	8.7	205.1	3.5
H_2	8.5	130.7	3.5
H_2O	9.9	188.8	4.0

provides improvement over the GGA+U functional, but still strongly underestimates the gap, whereas the HSE06 results agree with the GW results to within about 0.1 eV (see Table VII). Similar observations have been made for a wider range of materials [86]. Thus, the SCAN+U functional alone may not be sufficient to describe the charge equilibrium, but further research is needed to address this question quantitatively.

D. Gas phase equilibria

The conversion between partial pressures p (bar) and chemical potentials $\Delta\mu$ (eV) at a given temperature T (K) is calculated by taking standard conditions ($T^\circ = 298.15$ K, $p^\circ = 1$ bar) as the reference point and using the ideal gas law for temperatures higher than the ambient temperature and pressures lower than the ambient pressure:

$$\Delta\mu(T, p^\circ) = \left(H^\circ + c_p(T - T^\circ)\right) - T\left(S^\circ + c_p \ln(T/T^\circ)\right). \quad (7)$$

The standard enthalpies H° and entropies S° used here are given in Table VIII [74]. For ideal gases, the constant-pressure heat capacity depends only on the number of degrees of freedom, $c_p = (1 + n_{DOF}/2)k_B$ (see Table VIII), and the pressure dependence follows [87]

$$\Delta\mu(T, p) = \Delta\mu(T, p^\circ) + k_B T \ln(p/p^\circ). \quad (8)$$

Further using the tabulated 0-K formation enthalpy of water vapor [74], we can express the gas phase equilibrium as $\Delta H_f(H_2O) = 2\Delta\mu_H + \Delta\mu_O - \Delta\mu_{H_2O} = -2.476$ eV. Using $\Delta\mu_O = \frac{1}{2}\Delta\mu_{O_2}$ and $\Delta\mu_H = \frac{1}{2}\Delta\mu_{H_2}$ in conjunction with Eqs. (7) and (8) allows us to solve the relationships between pH_2, pO_2, and pH_2O for a given temperature.

IV. CONCLUSIONS

We introduced an approach for calculating thermochemical equilibria in the presence of repulsive defect interactions at high, nondilute concentrations. Constructing supercells of small to moderate size, we enumerated all nonequivalent defect-pair and defect-triplet configurations, and determined the distribution of energies from first-principles calculations. On the basis of these data,

we evaluated and parameterized the free energy of defect interaction, which depends on both defect concentration and temperature and which accounts for both enthalpy and configurational entropy contributions arising from the defect interactions. With use of total energies obtained with the SCAN+U functional, the interacting-defects approach yields near-quantitative agreement with experimental thermogravimetric data for $Sr_{1-x}Ce_xMnO_{3-\delta}$, whereas the off-stoichiometry is vastly overestimated in the noninteracting defect model. For pure $SrMnO_3$, we were able to show that minor adjustments to the SCAN+U-calculated V_O formation energies in the dilute limit, by less than 0.2 eV, bring the present model into full agreement with experiment over the entire temperature range up to 1700 °C. Simulating thermochemical water splitting with this approach, we find that Ce alloying in $SrMnO_3$ increases somewhat the critical H_2:H_2O ratio for net H_2 production, but affords minute, if any, gains in H_2 yield. More generally, defect interactions tend to suppress the (differential) reduction entropy, which lowers the H_2:H_2O ratio at the gas splitting (oxidation) step. The present approach advances simulation capabilities for materials and applications that rely on large off-stoichiometries where repulsive defect interactions become a decisive factor in the quantitative modeling of defect equilibria.

[1] *Key World Energy Statistics* (International Energy Agency, 2021).

[2] S. R. Kurtz, A. M. Leilaeioun, R. R. King, I. M. Peters, M. J. Heben, W. K. Metzger, and N. M. Haegel, Revisiting the terawatt challenge, MRS Bull. **45**, 159 (2020).

[3] A. H. McDaniel, Renewable energy carriers derived from concentrating solar power and nonstoichiometric oxides, Curr. Opin. Green Sustain. Chem. **4**, 37 (2017).

[4] Energy materials screening with defect graph neural networks, Nat. Comput. Sci. **3**, 671 (2023).

[5] K. J. Warren and A. W. Weimer, Solar thermochemical fuels: Present status and future prospects, Solar Compass **1**, 100010 (2022).

[6] W. C. Chueh and S. M. Haile, A thermochemical study of ceria: Exploiting an old material for new modes of energy conversion and CO_2 mitigation, Philos. Trans. R. Soc. London, A **368**, 3269 (2010).

[7] A. H. McDaniel, E. C. Miller, D. Arifin, A. Ambrosini, E. N. Coker, R. O'Hayre, W. C. Chueh, and J. Tong, Sr-and Mn-doped $LaAlO_{3-\delta}$ for solar thermochemical H_2 and CO production, Energy Environ. Sci. **6**, 2424 (2013).

[8] D. R. Barcellos, M. D. Sanders, J. Tong, A. H. McDaniel, and R. P. O'Hayre, $BaCe_{0.25}Mn_{0.75}O_{3-\delta}$—a promising perovskite-type oxide for solar thermochemical hydrogen production, Energy Environ. Sci. **11**, 3256 (2018).

[9] S. Zhai, J. Rojas, N. Ahlborg, K. Lim, M. F. Toney, H. Jin, W. C. Chueh, and A. Majumdar, The use of polycation oxides to lower the temperature of two-step thermochemical water splitting, Energy Environ. Sci. **11**, 2172 (2018).

[10] X. Qian, J. He, E. Mastronardo, B. Baldassarri, W. Yuan, C. Wolverton, and S. M. Haile, Outstanding properties and performance of $CaTi_{0.5}Mn_{0.5}O_{3-\delta}$ for solar-driven thermochemical hydrogen production, Matter **4**, 688 (2021).

[11] R. B. Wexler, G. S. Gautam, R. T. Bell, S. Shulda, N. A. Strange, J. A. Trindell, J. D. Sugar, E. Nygren, S. Sainio, A. H. McDaniel, *et al.*, Multiple and nonlocal cation redox in Ca–Ce–Ti–Mn oxide perovskites for solar thermochemical applications, Energy Environ. Sci. **16**, 2550 (2023).

[12] G. Sai Gautam, E. B. Stechel, and E. A. Carter, Exploring Ca–Ce–M–O ($M = 3d$ transition metal) oxide perovskites for solar thermochemical applications, Chem. Mater. **32**, 9964 (2020).

[13] D. R. Barcellos, F. G. Coury, A. Emery, M. Sanders, J. Tong, A. McDaniel, C. Wolverton, M. Kaufman, and R. O'Hayre, Phase identification of the layered perovskite $Ce_xSr_{2-x}MnO_4$ and application for solar thermochemical water splitting, Inorg. Chem. **58**, 7705 (2019).

[14] A. M. Bergeson-Keller, M. D. Sanders, and R. P. O'Hayre, Reduction thermodynamics of $Sr_{1-x}Ce_xMnO_3$ and $Ce_xSr_{2-x}MnO_4$ perovskites for solar thermochemical hydrogen production, Energy Technol. **10**, 2100515 (2022).

[15] A. A. Emery and C. Wolverton, High-throughput DFT calculations of formation energy, stability and oxygen vacancy formation energy of ABO_3 perovskites, Sci. Data. **4**, 1 (2017).

[16] R. B. Wexler, G. S. Gautam, E. B. Stechel, and E. A. Carter, Factors governing oxygen vacancy formation in oxide perovskites, J. Am. Chem. Soc. **143**, 13212 (2021).

[17] Z. J. Bare, R. J. Morelock, and C. B. Musgrave, A computational framework to accelerate the discovery of perovskites for solar thermochemical hydrogen production: Identification of Gd perovskite oxide redox mediators, Adv. Funct. Mater. **32**, 2200201 (2022).

[18] M. D. Witman, A. Goyal, T. Ogitsu, A. H. McDaniel, and S. Lany, Defect graph neural networks for materials discovery in high-temperature clean-energy applications, Nat. Comput. Sci. **3**, 675 (2023).

[19] G. Sai Gautam, E. B. Stechel, and E. A. Carter, A first-principles-based sub-lattice formalism for predicting off-stoichiometry in materials for solar thermochemical applications: The example of ceria, Adv. Theory Simul. **3**, 2000112 (2020).

[20] S. L. Millican, J. M. Clary, C. B. Musgrave, and S. Lany, Redox defect thermochemistry of $FeAl_2O_4$ hercynite in water splitting from first-principles methods, Chem. Mater. **34**, 519 (2022).

[21] B. Meredig and C. Wolverton, First-principles thermodynamic framework for the evaluation of thermochemical H_2O- or CO_2-splitting materials, Phys. Rev. B **80**, 245119 (2009).

[22] S. Lany, Communication: The electronic entropy of charged defect formation and its impact on thermochemical redox cycles, J. Chem. Phys. **148**, 071101 (2018).

[23] S. Zhang and J. E. Northrup, Chemical potential dependence of defect formation energies in GaAs: Application to Ga self-diffusion, Phys. Rev. Lett. **67**, 2339 (1991).

[24] S. Lany and A. Zunger, Dopability, intrinsic conductivity, and nonstoichiometry of transparent conducting oxides, Phys. Rev. Lett. **98**, 045501 (2007).

[25] S. L. Millican, A. M. Deml, M. Papac, A. Zakutayev, R. O'Hayre, A. M. Holder, C. B. Musgrave, and V. Stevanovic, Predicting oxygen off-stoichiometry and hydrogen incorporation in complex perovskite oxides, Chem. Mater. **34**, 510 (2022).

[26] S. Lany and A. Zunger, Light-and bias-induced metastabilities in $Cu(In, Ga)Se_2$ based solar cells caused by the (V_{Se}-V_{Cu}) vacancy complex, J. Appl. Phys. **100**, 113725 (2006).

[27] K. Biswas and S. Lany, Energetics of quaternary III-V alloys described by incorporation and clustering of impurities, Phys. Rev. B **80**, 115206 (2009).

[28] V. Stevanović, A. Zakutayev, and S. Lany, Composition dependence of the band gap and doping in Cu_2O-based alloys as predicted by an extension of the dilute-defect model, Phys. Rev. Appl. **2**, 044005 (2014).

[29] J. Pan, J. Cordell, G. J. Tucker, A. C. Tamboli, A. Zakutayev, and S. Lany, Interplay between composition, electronic structure, disorder, and doping due to dual sublattice mixing in nonequilibrium synthesis of $ZnSnN_2 : O$, Adv. Mater. **31**, 1807406 (2019).

[30] J. Ma and S.-H. Wei, Bowing of the defect formation energy in semiconductor alloys, Phys. Rev. B **87**, 241201 (2013).

[31] J. Park, B. Xu, J. Pan, D. Zhang, S. Lany, X. Liu, J. Luo, and Y. Qi, Accurate prediction of oxygen vacancy concentration with disordered A-site cations in high-entropy perovskite oxides, npj Comput. Mater. **9**, 29 (2023).

[32] C. B. Gopal and A. van de Walle, Ab initio thermodynamics of intrinsic oxygen vacancies in ceria, Phys. Rev. B **86**, 134117 (2012).

[33] T. Das, J. D. Nicholas, and Y. Qi, Polaron size and shape effects on oxygen vacancy interactions in lanthanum strontium ferrite, J. Mater. Chem. A **5**, 25031 (2017).

[34] V. I. Anisimov, J. Zaanen, and O. K. Andersen, Band theory and mott insulators: Hubbard *U* instead of Stoner *I*, Phys. Rev. B **44**, 943 (1991).

[35] A. D. Becke, A new mixing of Hartree–Fock and local density-functional theories, J. Chem. Phys. **98**, 1372 (1993).

[36] P. Wei and Z. Q. Qi, Insulating gap in the transition-metal oxides: A calculation using the local-spin-density approximation with the on-site Coulomb *U* correlation correction, Phys. Rev. B **49**, 10864 (1994).

[37] M. Marsman, J. Paier, A. Stroppa, and G. Kresse, Hybrid functionals applied to extended systems, J. Phys.: Condens. Matter **20**, 064201 (2008).

[38] H. Peng and S. Lany, Polymorphic energy ordering of MgO, ZnO, GaN, and MnO within the random phase approximation, Phys. Rev. B **87**, 174113 (2013).

[39] K. Saritas, J. T. Krogel, and F. A. Reboredo, Relative energies and electronic structures of CoO polymorphs through ab initio diffusion quantum Monte Carlo, Phys. Rev. B **98**, 155130 (2018).

[40] J. Sun, A. Ruzsinszky, and J. P. Perdew, Strongly constrained and appropriately normed semilocal density functional, Phys. Rev. Lett. **115**, 036402 (2015).

[41] S. L. Dudarev, G. A. Botton, S. Y. Savrasov, C. J. Humphreys, and A. P. Sutton, Electron-energy-loss spectra and the structural stability of nickel oxide: An LSDA+U study, Phys. Rev. B **57**, 1505 (1998).

[42] A. Daoud-Aladine, C. Martin, L. Chapon, M. Hervieu, K. Knight, M. Brunelli, and P. Radaelli, Structural phase transition and magnetism in hexagonal $SrMnO_3$ by magnetization measurements and by electron, X-ray, and neutron diffraction studies, Phys. Rev. B **75**, 104417 (2007).

[43] D. A. Keen and A. L. Goodwin, The crystallography of correlated disorder, Nature **521**, 303 (2015).

[44] R. Søndenå, S. Stølen, P. Ravindran, T. Grande, and N. L. Allan, Corner-versus face-sharing octahedra in $AMnO_3$ perovskites (A = Ca, Sr, and Ba), Phys. Rev. B **75**, 184105 (2007).

[45] T. Negas and R. S. Roth, The system $SrMnO_{3-x}$, J. Solid. State. Chem. **1**, 409 (1970).

[46] L. Rørmark, A. B. Mørch, K. Wiik, S. Stølen, and T. Grande, Enthalpies of oxidation of $CaMnO_{3-\delta}$, $Ca_2MnO_{4-\delta}$ and $SrMnO_{3-\delta}$——deduced redox properties, Chem. Mater. **13**, 4005 (2001).

[47] A. Sharan and S. Lany, Computational discovery of stable and metastable ternary oxynitrides, J. Chem. Phys. **154**, 234706 (2021).

[48] T. Takeda and S. Ohara, Magnetic structure of the cubic perovskite type $SrMnO_3$, J. Phys. Soc. Jpn. **37**, 275 (1974).

[49] See Supplemental Material at http://link.aps.org/supplemental/10.1103/PRXEnergy.3.013008 for Fig. S1 (Sr-Mn-O phase diagram), Table S1 (SCAN+*U*-predicted compound formation enthalpies), Fig. S2 (theory-experiment comparison), Fig. S3 (redox couples for determination of the *U* parameter), and Fig. S4 (extrapolation of defect formation energies). Also included is a compressed archive containing the crystallographic structure files of the relaxed SCAN+*U* structures of $SrMnO_3$ and the SCM alloy SQS, as well as thermodynamic data shown in Figs. 2 and 6, along with the codes used to generate the data,

[50] including the implementation of the ideal gas law equations in Sec. III D.

H. T. Stokes and D. M. Hatch, FINDSYM: Program for identifying the space-group symmetry of a crystal, J. Appl. Crystallogr. **38**, 237 (2005).

[51] H. Peng, D. O. Scanlon, V. Stevanovic, J. Vidal, G. W. Watson, and S. Lany, Convergence of density and hybrid functional defect calculations for compound semiconductors, Phys. Rev. B—Condens. Matter Mater. Phys. **88**, 1 (2013).

[52] S. Zhang, S.-H. Wei, and A. Zunger, Stabilization of ternary compounds via ordered arrays of defect pairs, Phys. Rev. Lett. **78**, 4059 (1997).

[53] P. Dalach, D. Ellis, and A. Van De Walle, First-principles thermodynamic modeling of atomic ordering in yttria-stabilized zirconia, Phys. Rev. B **82**, 144117 (2010).

[54] J. Pan, J. J. Cordell, G. J. Tucker, A. Zakutayev, A. C. Tamboli, and S. Lany, Perfect short-range ordered alloy with line-compound-like properties in the $ZnSnN_2$:ZnO system, npj Comput. Mater. **6**, 1 (2020).

[55] A. Goyal, A. Zakutayev, V. Stevanović, and S. Lany, Computational Fermi level engineering and doping-type conversion of Mg : Ga_2O_3 via three-step synthesis process, J. Appl. Phys. **129**, 245704 (2021).

[56] N. A. Strange, J. E. Park, A. Goyal, R. T. Bell, J. A. Trindell, J. D. Sugar, K. H. Stone, E. N. Coker, S. Lany, S. Shulda, *et al.*, Formation of $6H$-$Ba_3Ce_{0.75}Mn_{2.25}O_9$ during thermochemical reduction of $12R$-$Ba_4CeMn_3O_{12}$: Identification of a polytype in the Ba(Ce, Mn)O_3 family, Inorg. Chem. **61**, 6128 (2022).

[57] A. F. Fuentes, K. Boulahya, and U. Amador, Novel rare-earth-containing manganites $Ba_4REMn_3O_{12}$ (RE = Ce, Pr) with $12R$ structure, J. Solid. State. Chem. **177**, 714 (2004).

[58] S. Hashimoto and H. Iwahara, Structural, thermal and electrical properties of Ce-doped $SrMnO_3$, J. Electroceram. **4**, 225 (2000).

[59] A. Sundaresan, J. Tholence, A. Maignan, C. Martin, M. Hervieu, B. Raveau, and E. Suard, Jahn-Teller distortion and magnetoresistance in electron doped $Sr_{1-x}Ce_xMnO_3$ (x = 0.1, 0.2, 0.3 and 0.4), Eur. Phys. J. B-Condens. Matter Complex Syst. **14**, 431 (2000).

[60] A. Zunger, S.-H. Wei, L. G. Ferreira, and J. E. Bernard, Special quasirandom structures, Phys. Rev. Lett. **65**, 353 (1990).

[61] H. Wu, K. Ruan, S. Huang, Z. Lv, and L. Cao, Intrinsic inhomogeneity in the electron-doped manganite $Sr_{0.95}Ce_{0.05}MnO_3$, Solid. State. Commun. **141**, 198 (2007).

[62] S. S. Naghavi, A. A. Emery, H. A. Hansen, F. Zhou, V. Ozolins, and C. Wolverton, Giant onsite electronic entropy enhances the performance of ceria for water splitting, Nat. Commun. **8**, 285 (2017).

[63] D. Zhang, H. A. De Santiago, B. Xu, C. Liu, J. A. Trindell, W. Li, J. Park, M. A. Rodriguez, E. N. Coker, J. D. Sugar, *et al.*, Compositionally complex perovskite oxides for solar thermochemical water splitting, Chem. Mater. **35**, 1901 (2023).

[64] P. E. Blöchl, Projector augmented-wave method, Phys. Rev. B **50**, 17953 (1994).

[65] G. Kresse, From ultrasoft pseudopotentials to the projector augmented-wave method, Phys. Rev. B **59**, 1758 (1999).

[66] G. Kresse and J. Furthmüller, Efficiency of ab-initio total energy calculations for metals and semiconductors using a plane-wave basis set, Comput. Mater. Sci. **6**, 15 (1996).

[67] J. P. Perdew, K. Burke, and M. Ernzerhof, Generalized gradient approximation made simple, Phys. Rev. Lett. **77**, 3865 (1996).

[68] J. Heyd, G. E. Scuseria, and M. Ernzerhof, Hybrid functionals based on a screened Coulomb potential, J. Chem. Phys. **118**, 8207 (2003).

[69] J. Heyd, G. E. Scuseria, and M. Ernzerhof, Erratum: "Hybrid functionals based on a screened Coulomb potential" [J. Chem. Phys. 118, 8207 (2003)], J. Chem. Phys. **124**, 219906 (2006).

[70] V. Stevanović, S. Lany, X. Zhang, and A. Zunger, Correcting density functional theory for accurate predictions of compound enthalpies of formation: Fitted elemental-phase reference energies, Phys. Rev. B **85**, 115104 (2012).

[71] G. S. Gautam and E. A. Carter, Evaluating transition metal oxides within DFT-SCAN and SCAN+U frameworks for solar thermochemical applications, Phys. Rev. Mater. **2**, 095401 (2018).

[72] S. Lany, Semiconductor thermochemistry in density functional calculations, Phys. Rev. B **78**, 245207 (2008).

[73] C. J. Bartel, A. W. Weimer, S. Lany, C. B. Musgrave, and A. M. Holder, The role of decomposition reactions in assessing first-principles predictions of solid stability, npj Comput. Mater. **5**, 4 (2019).

[74] D. D. Wagman, W. H. Evans, V. B. Parker, R. H. Schumm, and I. Halow, *The NBS tables of chemical thermodynamic properties. Selected values for inorganic and C1 and C2 organic substances in SI units*, Tech. Rep. (National Standard Reference Data System, 1982).

[75] D. Sedmidubsky, A. Strejc, M. Nevřiva, J. Leitner, and C. Martin, Structural and phase relations in the Sr-Mn-O system, Solid State Phenom. **90**, 427 (2003).

[76] E. Cordfunke, A. Booij, and M. Huntelaar, The thermochemical properties of $BaCeO_3$ (s) and $SrCeO_3$ (s) from T = (5 to 1500) K, J. Chem. Thermodyn. **30**, 437 (1998).

[77] L. Hedin, New method for calculating the one-particle Green's function with application to the electron-gas problem, Phys. Rev. **139**, A796 (1965).

[78] M. Shishkin and G. Kresse, Implementation and performance of the frequency-dependent GW method within the PAW framework, Phys. Rev. B **74**, 035101 (2006).

[79] NREL materials database, https://materials.nrel.gov.

[80] S. Lany, Band-structure calculations for the $3d$ transition metal oxides in *GW*, Phys. Rev. B **87**, 085112 (2013).

[81] S. Lany, Semiconducting transition metal oxides, J. Phys.: Condens. Matter **27**, 283203 (2015).

[82] K. K. Irikura, Experimental vibrational zero-point energies: Diatomic molecules, J. Phys. Chem. Ref. Data **36**, 389 (2007).

[83] J. Klarbring and S. I. Simak, Nature of the octahedral tilting phase transitions in perovskites: A case study of $CaMnO_3$, Phys. Rev. B **97**, 024108 (2018).

[84] A. Goyal, P. Gorai, H. Peng, S. Lany, and V. Stevanović, A computational framework for automation of point defect calculations, Comput. Mater. Sci. **130**, 1 (2017).

[85] A. Van De Walle, M. Asta, and G. Ceder, The alloy theoretic automated toolkit: A user guide, CALPHAD **26**, 539 (2002).

[86] P. Borlido, T. Aull, A. W. Huran, F. Tran, M. A. Marques, and S. Botti, Large-scale benchmark of exchange–correlation functionals for the determination of electronic band gaps of solids, J. Chem. Theory Comput. **15**, 5069 (2019).

[87] K. Reuter and M. Scheffler, Composition, structure, and stability of RuO_2 (110) as a function of oxygen pressure, Phys. Rev. B **65**, 035406 (2001).